Journal of Materials Chemistry C

ROYAL SOCIETY OF CHEMISTRY

PAPER

View Article Online
View Journal | View Issue

Cite this: J. Mater. Chem. C, 2021, 9, 11331

Mechanism of electrochemical oxygen reduction reaction at two-dimensional Pt-doped $MoSe_2$ material: an efficient electrocatalyst

Shrish Nath Upadhyay [a] and Srimanta Pakhira *[abc]

The O_2 reduction reaction (ORR) is a promising reaction in clean energy conversion systems such as fuel cells, metal–air batteries, and electrochemical reactions. Pt shows excellent electrocatalytic activities for ORR, but their high cost and poor durability hinder their wide application in electrochemistry for energy conversion. In this work, we have computationally designed a 2D monolayer Pt-doped $MoSe_2$ (noted by Pt–$MoSe_2$) material, and studied the structural and electronic properties with the ORR activities within the framework of first principles-based periodic hybrid Density Functional Theory (DFT). After doping the Pt atom in the pristine 2D monolayer $MoSe_2$ material, it became metallic with zero band gap and considerable electronic states at the Fermi energy (E_F) level, which were confirmed by performing the band structure and total density of states (DOS) calculations. A detailed reaction mechanism based on thermodynamic analysis of ORR on the surfaces of the 2D monolayer Pt–$MoSe_2$ material was carried out by performing quantum mechanical DFT calculations. We explored the electrocatalytic performance of the 2D monolayer Pt–$MoSe_2$ towards ORR, and full ORR pathways and reaction mechanism by computing the relative Gibb's free energy (ΔG) at the same DFT method. The present study shows how to design better electrocatalysts for ORR by understanding the chemical basis for Pt-doping in $MoSe_2$ and modification of the 2D layer structure, which paves the way to create high-performance and easily-accessible electrocatalysts. This work indicates that the 2D monolayer Pt–$MoSe_2$ is a promising candidate to substitute Pt electrodes, and an excellent electrocatalyst for fuel cell components in future applications.

Received 12th May 2021,
Accepted 21st July 2021

DOI: 10.1039/d1tc02193a

rsc.li/materials-c

Introduction

The search for renewable and green energy sources to replace the conventional sources of energy has drawn considerable attention of researchers in modern science and technology. At present, most of the energy demands of our society are being fulfilled by conventional energy sources (*i.e.*, coal, petroleum, CNG), which produce greenhouse gases. The large-scale exploitation of conventional energy sources, such as fossil fuels, affects the environment by pollution. Addressing the issues of global climate change and high energy demands require novel approaches in clean and green energy generation, high-capacity energy devices, and efficient manufacturing. Fuel cells and metal–air batteries are some of the most promising solutions for future energy demands in various applications, including electric vehicles, solar cells.[1,2] Fuel cells convert chemical energy into electricity through electrochemical reactions. These advanced energy technologies involve the reduction of oxygen as one of the electrode reactions.[3–5] Oxygen reduction reactions (ORR) are well studied cathodic reactions in fuel cells.[6,7] ORR can be done *via* two possible mechanisms, either a two-electron transfer reaction that gives H_2O_2 as a product or four-electron transfer reaction producing H_2O.[8] The number of electrons transferred during ORR is based on the nature and activity of the selected electrocatalyst. For platinum-based catalysts, the four-electron transfer mechanism is the dominating phenomenon.[9]

$$\text{Four-electron route:}\quad O_2 + 4H^+ + 4e^- \rightarrow 2H_2O \qquad E^\circ_{cell} = 1.23\ \text{V} \tag{1}$$

$$\text{Two-electron route:}\quad O_2 + 2H^+ + 2e^- \rightarrow H_2O_2 \qquad E^\circ_{cell} = 0.695\ \text{V} \tag{2}$$

here, E°_{cell} is the standard electrode potential of the cell. It is the difference of the two electrodes, which forms the voltage of

[a] Department of Metallurgy Engineering and Materials Science (MEMS), Indian Institute of Technology Indore, Simrol, Khandwa Road, Indore-453552, MP, India. E-mail: spakhira@iiti.ac.in, spakhirafsu@gmail.com
[b] Department of Physics, Indian Institute of Technology Indore (IITI), Simrol, Khandwa Road, Indore-453552, MP, India
[c] Centre for Advanced Electronics (CAE), Indian Institute of Technology Indore, Simrol, Khandwa Road, Indore-453552, MP, India

that cell. The value of E°_{cell} can be obtained using the following equation.

$$E^{\circ}_{cell} = E^{\circ}_{cathode} - E^{\circ}_{electrode} \quad (3)$$

The kinetics of the cathodic O_2 reduction reactions are much slower than those of the anodic reactions. This is the main drawback of ORR fuel cells, which presents a bottleneck for the overall cell performance.[10] To speed up the kinetics of the ORR, an efficient electrocatalyst is required. Currently, the dominating catalyst used for ORR is platinum group metal elements (PGM). They are the most favorable ORR electrocatalysts, displaying the absolute superiority of catalytic activity. Among them, Pt is the best electrocatalyst known to date, but it is far from being ideal.[11] However, the high cost, poor stability/durability, low poison resistance of PGM hinder their large-scale applications and commercialization. Some non-Pt based electrocatalysts have also been explored in recent years, but their stability and catalytic performance are not up to that of the Pt-based electrocatalysts. For the viable development of fuel cells, it is important to reduce the amount of Platinum in the Pt-based catalysts without losing the catalytic activity.[12]

ORR is quite sensitive to the electronic properties and atomic arrangement or coordination of the surface of the catalyst. Hence, modifying the surface properties, including the electronic structure and atomic arrangement of the catalyst's surface, will effectively tune the catalytic activity of the Pt-based catalyst, enhancing both activity and durability.[13] In response to this, modified electronic properties improve the O_2 adsorption activity. This adsorption behavior is believed to be the origin of the high activity for ORR. Recently, two-dimensional (2D) materials have attracted the attention of researchers for the development of efficient catalysts for ORR.[14] The 2D materials have different properties from their bulk structures, such as the high surface area and surface to volume ratio, which plays an important role in their electrocatalytic activity.[15] A positive approach in this direction is the doping of transition metals into the pristine 2D materials. The single atom doping site acts as an active center that favors the ORR by enhancing the catalytic activity, and can help in the search for a new electrocatalyst for ORR. Single-atom catalysts can provide active sites that can be tuned, and promise the doping of fewer amounts of transition metals. This area of research has become quite intense these days.[16] The development of a new catalyst has mainly been inspired by chemical intuition and experimental observations. However, computational studies are also being employed to this effort. Density functional theory (DFT) calculations have proved to be a useful technique to design new catalysts for ORR and HER. DFT calculations can provide knowledge about the stability of surface intermediates in the reactions that cannot be determined easily by other means. Recently, several electrocatalytic materials have been developed by using DFT methods to investigate the kinetics of ORR.[11,17,18]

After the discovery and extensive studies of several 2D materials, various research groups have reported on 2D thin nanosheets and even monolayers with platinum doping, which shows excellent ORR activity compared to the commercial Pt/C catalysts.[19,20] The 2D Pt-based chalcogenides (*e.g.*, $PtSe_2$, PtS_2) have been synthesized, and their properties and possible applications for ORR have been experimentally studied.[21] Grønvold *et al.* reported that Pt can bind with the chalcogens to form 2D dichalcogenides.[22] These dichalcogenides with Pt doping were found to be semiconducting (as there was no electron density of states at the Fermi energy level). Hence, they are intrinsically inert for ORR.[23–25] However, most of these Pt-based catalysts are supported on the other noble metals (*e.g.*, Au, Pd). Among the various 2D materials studied for H_2 evolution reactions (HER) as an electrocatalyst, the family of 2D transition metal dichalcogenides (TMDs)[26–28] are being extensively studied as alternative electrocatalysts due to their peculiar electronic properties and crystal structure.[26] Transition metals show variable valence. Hence, they can easily form unstable reaction intermediates. That is why they can be used as an electrocatalyst. These TMDs are also earth-abundant, cheap, cost effective, and efficient for electrocatalytic activity towards HER, and also possible for ORR.[12] The basal planes of TMDs are inert; hence, they cannot be used as an electrocatalyst for ORR. To activate their inert basal plane, it is necessary to dope them with some noble metal atoms, like Pt or Pd.[26] Electrocatalysts containing a large amount of pure noble metal atoms cannot be commercialized due to the metal scarcity and high cost of these metals. Researchers are trying to minimize the Pt percentage or even to remove it completely from the TMDs-based electrocatalysts, which can efficiently reduce O_2 during the oxygen reduction reaction. The 2D monolayer pristine $MoSe_2$ is a rising star in the family of 2D TMDs, whose tunable band gap makes it a promising candidate for various applications. The layered structure of the 2D pristine $MoSe_2$, plus the size and electrical conductivity of Se, provide a good opportunity for hosting counter ions in electrochemical energy storage systems, such as lithium-ion and sodium-ion batteries.[29] However, the basal planes of TMDs are usually inert. Hence, they cannot be an efficient catalyst, except for the exposed edges of the TMDs.[30] The key point here is to activate the basal plane of the TMDs, so that it can be further used in electrocatalytic reactions as an efficient electrocatalyst. We hypothesize that the Pt-doped 2D monolayer $MoSe_2$ material would be a potential electrocatalyst for ORR with the doping of a single Pt atom, *i.e.*, 25% of the Pt atom per 2×2 supercell.

In this work, we have computationally designed 2D monolayer earth-abundant pristine $MoSe_2$ transition metal dichalcogenides (TMDs) and a Pt-doped $MoSe_2$ (Pt–$MoSe_2$) material, as shown in Fig. 1. The present study found that the pristine 2D monolayer $MoSe_2$ material is a high band gap semiconductor with a large electronic band gap about 2.21 eV. Its limited number of catalytically active sites for the ORR hinders its practical application. Hence, it cannot be used as a suitable electrocatalyst for ORR. In the special case of electrochemical reactions, such as ORR (where the electrons are reactants), the electric conductivity is a more important consideration than for general chemical reactions. The 2D monolayer $MoSe_2$ does not exhibit sufficiently high conductivity, which obstructs electron

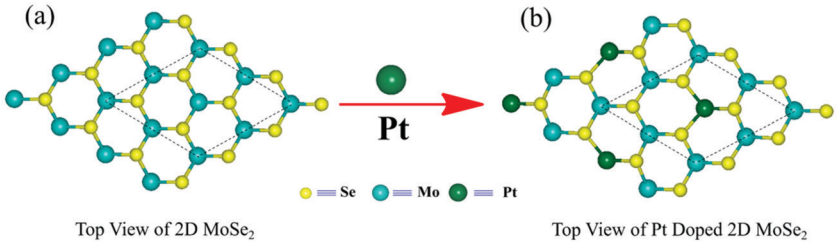

Fig. 1 (a) The top view of the periodic layer structure of the pristine 2D monolayer $MoSe_2$ and (b) the top view of the periodic 2D layer structure of the platinum-doped $MoSe_2$ (Pt–$MoSe_2$) material are presented here. (The 2 × 2 supercell boundary is represented with a dotted line.)

transfer during the ORR process as the 2D monolayer $MoSe_2$ is a pure high band gap semiconductor. Our computational study reveals that the Pt doping increases the conductivity of $MoSe_2$ by decreasing the electronic band gap from 2.21 eV to 0 eV, and the total DOS calculations indicate that a large electron density has appeared at the Fermi energy level (E_F) due the Pt-doping in the pristine 2D monolayer $MoSe_2$. The Pt atom doping increases the carrier concentration, which enhances the electronic conductivity. Therefore, a better catalytic activity is expected for the oxygen reduction efficiency, suggesting a novel approach to enhance the ORR performance of the Pt-doped $MoSe_2$ 2D material. The ORR mechanism has been studied on the surface of the 2D monolayer Pt–$MoSe_2$ material, and the various reaction steps occurring in the reactions were computed, along with the changes of free energy and the band structure and DOS during the reactions. The present study leads us to report that the 2D monolayer Pt–$MoSe_2$ material is an excellent catalyst for ORR.

Methods and computational details

The advancement in the current scenario of materials science provides a better understanding to examine the role of a catalyst with molecules/atoms at a microscopic scale. In comparison to other row elements of the periodic table, it is difficult to study the transition metal-based catalysts.[31] Recent advancements in plane-wave basis sets, Gaussian types of basis sets and Gaussian type of orbitals (GTO), pseudo potential, and ultra-fast supercomputers have made computations easier for exploring the surface phenomenon of different catalysts, investigating various catalytic activities and reaction mechanisms.[32] To understand the adsorption behavior of an atom on a catalytic surface properly, the reaction barrier plays a key role, which gives the clue of uses of catalyst in various electrocatalytic applications.[33] To explore the reaction pathway and mechanism of ORR, we have used the first principles-based periodic hybrid DFT method. It is an excellent computing method based on quantum mechanics to study the various properties, such as thermodynamic properties, electronic properties, and reaction mechanisms of 2D layer structures.[34,35]

(a) Material preparation

The equilibrium 2D pristine $MoSe_2$ monolayer structure was obtained by applying the first principles-based periodic dispersion-corrected hybrid density functional theory (DFT-D) method.[34,35] The unit cell of the equilibrium 2D pristine $MoSe_2$ was increased to 2 × 2 supercell, and one Mo atom was replaced by the Pt atom in the 2 × 2 supercell of $MoSe_2$ to prepare the 2D Pt-doped $MoSe_2$ (noted by Pt–$MoSe_2$) monolayer material. In other words, to develop the 2D Pt-doped $MoSe_2$ monolayer material, we took a hexagonal symmetric 2D $MoSe_2$ and created a 2 × 2 supercell slab model. Then, we replaced one of the Mo atoms with a single Pt atom in the 2 × 2 pristine $MoSe_2$ 2D slab. A theoretical and computational study was performed to obtain the equilibrium structure and electronic properties (band structure and density of states (DOS)) of both 2D monolayer $MoSe_2$ and Pt–$MoSe_2$ materials using the same DFT-D method. The equilibrium geometry of the 2D $MoSe_2$ was optimized to be $a = b = 3.234$ Å with space group "$P\bar{6}m2$". For the Pt-doped $MoSe_2$, the equilibrium lattice constants were found to be $a = b = 6.738$ Å with space-group symmetry "$P1$".

(b) Periodic DFT calculations

Equilibrium structures of all unit cells were obtained by using the first principles-based periodic hybrid density functional theory (DFT) method B3LYP[36–38] implemented in the CRYSTAL17 suite code.[32,34,37] The atomic basis set used in this CRYSTAL17 program is Gaussian-type (GTO, *i.e.*, Gaussian-type orbitals), which is a more effective basis set for the hybrid DFT calculations than plane waves.[27,39–43] Triple-ζ valence with polarization quality (TZVP) Gaussian basis sets were used for the O, H, Mo and Se atoms and Pt_doll_2004 basis set with the relativistic effective core potentials (ECPs) for the Pt atom in the present computations. Since there are many weak van der Waals (vdW) interactions between the layers of both $MoSe_2$ and Pt–$MoSe_2$ materials and among the atoms, it becomes necessary to describe the weak van der Waals (vdW) dispersion effects.[26,42–47] To account for all of the long-range vdW interactions, the semi-empirical Grimme's 3rd order (-D3) corrections of dispersion have been included in this present study. DFT-D (*i.e.*, B3LYP-D3) is a very useful method that not only gives the nice geometry of the 2D structure, but the energy and density are also less affected by the spin contaminations in the present computation.[48–50] The electronic self-consistency criterion was set to 10^{-7} a.u. in all of the calculations. For the consideration of the electrostatic potential in these calculations, two-dimensional (2D) vacuum slabs were developed for these materials and the energies were reported with respect to the vacuum. The height of the cell was formally set to 500 Å (no periodicity in the *z*-direction in the 2D slab model in

CRYSTAL17 code), *i.e.*, the vacuum region of approximately 500 Å was considered in the present calculations. This approach differs from the plane-wave codes (*e.g.*, VASP, Quantum Espresso); however, both reach similar results.[26,45] The DFT exchange–correlation contribution was evaluated by numerical integration over the unit cell volume. Radial and angular points of the integration grid were generated through Gauss–Legendre radial quadrature and Lebedev two-dimensional angular point distributions.[27,38]

After obtaining the equilibrium structures and geometries of both pristine 2D $MoSe_2$ and Pt–$MoSe_2$ monolayer materials, the electronic properties, *i.e.*, electronic band structures and density of states (DOS) were computed at the same level of theory. All integrations of the first Brillouin zone were sampled on $20 \times 20 \times 1$ Monkhorst–Pack[51] *k*-mesh grids for the pristine $MoSe_2$ and $4 \times 4 \times 1$ Monkhorst *k*-mesh grids for Pt–$MoSe_2$. The threshold for the convergence of energy, forces, and electron density was set to be 10^{-7} a.u. for evaluation. The *k*-vector path taken for plotting the band structure was selected as the highly symmetric *Γ–M–K–Γ* direction in the first Brillouin zone for both of the materials (*i.e.*, pristine $MoSe_2$ and Pt-doped $MoSe_2$). The atomic orbitals of the Mo, Se, O, H and Pt atoms were used to compute the total DOS. Electrostatic potential calculations were incorporated in the present study, which means that the energy for both the band structures and DOS is calculated with respect to vacuum (*i.e.*, w.r.t. vac.). For graphical representation and analysis of all of the optimized 2D layer structures, a visualization code (VESTA) was used.[52]

(c) ORR mechanism

To describe the O_2 reduction reaction network for the ORR, various elementary steps including different protonation states have been taken into consideration inspired by the method developed by Nørskov and coworkers.[44] The DFT calculations show that O_2 prefers to adsorb at the bridge sites on the Pt–$MoSe_2$ surface. Both $2e^-$ and $4e^-$ mechanisms have been included for the sequential reduction reactions of O_2. The dissociative and associative mechanism pathways are generally the following eqn (1) and (2), respectively.[7,8,12]

$$O_2 \rightarrow O_2^* \rightarrow 2O^* \rightarrow O^* + OH^* \rightarrow O^* + H_2O \text{ (or } H_2O_2) \rightarrow OH^* + H_2O \rightarrow 2H_2O \quad \text{(R1)}$$

$$O_2 \rightarrow O_2^* \rightarrow OOH^* \rightarrow O^* + H_2O \text{ (or } H_2O_2) \rightarrow OH^* + H_2 \rightarrow 2H_2 \quad \text{(R2)}$$

$$H^+ + OH^- \rightarrow H_2O \quad \text{(R3)}$$

where * denotes an adsorption site or active site of the catalyst. It should be noted that the protons and electrons have been left out for clarity. H_2O (or H_2O_2) is the product of the $2e^-$ ORR. It should be mentioned here that along the $4e^-$ pathway, O_2* is dissociated into 2O* on the surface of the 2D monolayer Pt–$MoSe_2$, and then reduced by H_2O (or H_2O_2) together with one electron transfer to form OH* at the top sites and a solvated OH^- anion. Here, we have focused on the dominating dissociative ORR mechanism pathway, as O_2 dissociation on the surface of the 2D Pt–$MoSe_2$ monolayer material is identified to be quite thermodynamically and energetically favorable, as followed by previous work on the ORR on the surface of the 2D PtTe monolayer.[12] Assuming the coupling between an electron transfer to the electrode, the formation of OH^- (more specifically $OH^- - e^-$ in our notation) was also expressed as $(H^+ + e^-) + (OH^- - e^-) \leftrightarrow H_2O$. Using the standard hydrogen electrode (SHE) as the reference electrode, the free energy of $OH^- - e^-$, $G(OH^- - e^-)$ was then determined by applying eqn (4)–(6) below.

(d) Theoretical calculations and equations

We used a 2×2 super cell and explored all of the reaction steps of ORR with respect to the computational hydrogen electrode model (CHE) or standard hydrogen electrode (SHE).[53] The free energy of each species can be expressed using the equation below:

$$G = E_{DFT} + E_{ZPE} + \int C_p dT - TS \quad (4)$$

where E_{DFT}, E_{ZPE} and S are the ground state electronic energy, zero-point vibrational energy and entropy, respectively. T is taken to be 298.15 K. The change in the free energy of reaction intermediates (adsorbates) has been calculated at pH = 0 using the following equation:

$$\Delta G_{ads} = \Delta E_{ads} + \Delta E_{ZPE} - T\Delta S \quad (5)$$

where ΔG_{ads} is the adsorption free energy of adsorbates, and ΔE_{ZPE} and ΔS are the difference of zero-point vibrational energy (E_{ZPE}) and entropy (S), respectively. The specific heat capacity contribution has been considered in the free energy (G) calculations (see eqn (4)). However, the lattice specific heat capacity C_p is fixed when the temperature (T) is kept at 298.15 K. For the change of free energy during the H-adsorption, the temperature (T) is constant. Thus, the integral part of the $\int C_p dT$ is zero when we calculated the changes of free energy during the ORR steps following eqn (5). The free energy of O_2 have been computed by the following equation, as the O_2 in the triplet ground state is notoriously and poorly described by the DFT methods.[12]

$$G_{O_2} = 2G_{H_2O} - 2G_{H_2} - 4.92 \text{ eV} \quad (6)$$

Results and discussions

The equilibrium structure (top view and side view with increased unit cell two times (2×2) in the *x*- and *y*-directions, and there is no change in the *z*-direction), band structure, and total density of states (DOS) of the pristine 2D $MoSe_2$ obtained by the B3LYP-D3 method are shown in Fig. 2a–c, respectively. Our present DFT-D study shows that the pristine 2D $MoSe_2$ has hexagonal $P\bar{6}m2$ symmetry with the equilibrium lattice constants $a = b = 3.234$ Å, $\alpha = \beta = 90^\circ$, and $\gamma = 120^\circ$, which are consistent with the previous experiment within 0.05 Å.[54] In other words, the present computed lattice constants are in good agreement with the experimental values of $a = b = 3.288$ Å observed by James and co-workers.[54] Kang and co-workers calculated the equilibrium lattice constants of the pristine 2D $MoSe_2$ and they found it to be

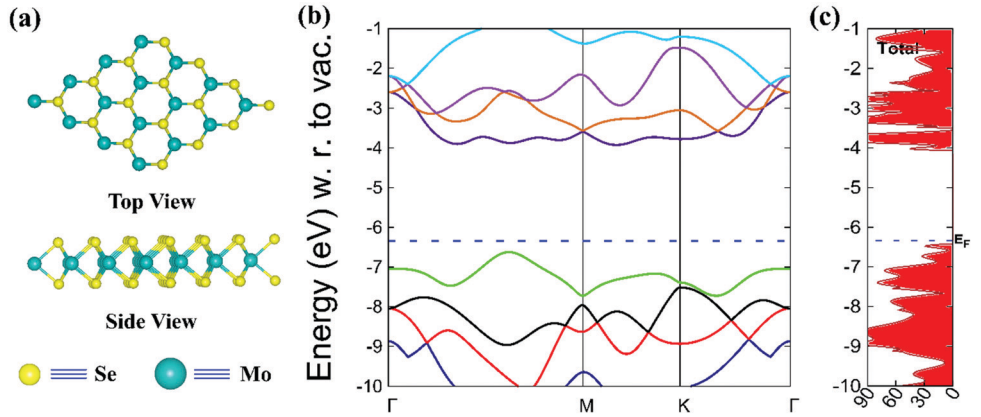

Fig. 2 The equilibrium 2D layer structure of the pristine $MoSe_2$ material: (a) top view and side view; (b) electronic band structure, and (c) total density of states (DOS) computed at the DFT-D level of theory are displayed.

$a = b = 3.250$ Å, which is in good agreement with our present DFT-D results.[55] The equilibrium Mo–Se bond distance was found to be 2.506 Å, computed by the DFT-D method, which is also in good agreement with the experimental results (2.490 Å).[54] The electronic band structures of the pristine $MoSe_2$ were plotted in the highly symmetric direction (*i.e.*, *Γ–M–K–Γ*) w.r.t. vacuum, as depicted in Fig. 2b, and the Fermi energy level (E_F) was found at −6.34 eV drawn in dotted blue line as shown in Fig. 2b. The number of four conduction bands and four valence bands have been computed and plotted around the Fermi level, and these band structure calculations show that the pristine 2D monolayer $MoSe_2$ has a direct bandgap of around 2.21 eV. The total electron density of states (DOS) has been computed at the same level of theory, as shown in Fig. 2(c), which confirms that the electronic band gap of the pristine 2D $MoSe_2$ is about 2.21 eV. There was no electron density around the Fermi level, which agrees well with the previous experiment and theory.[54] This result leads us to predict that the pristine 2D $MoSe_2$ cannot be used as an electrocatalyst to enhance the kinetics of ORR because it has a large band gap, making it a semiconductor.

The equilibrium 2D monolayer structure of the Pt–$MoSe_2$ material (2 × 2 supercell) was obtained by the same DFT-D method, as shown in Fig. 3(a), and the electronic properties calculations, *i.e.*, band structure and DOS of this material have been performed at the equilibrium geometry. The equilibrium lattice constants were found to be $a = b = 6.738$ Å, $\alpha = \beta = 90^\circ$ and $\gamma = 121.7^\circ$ with *P*1 symmetry. The adjacent angle was increased by an amount of 1.7° after doping Pt in the pristine $MoSe_2$, and the lattice constants have been increased in Pt–$MoSe_2$. The equilibrium lattice parameters $a = b = 6.738$ Å were increased by an amount of 0.270 Å from twice the value (6.468 Å) of the optimized lattice parameters of the pristine $MoSe_2$. The equilibrium Mo–Se bond distance in the Pt–$MoSe_2$ was found to be 2.518 Å, which is 0.012 Å larger than the equilibrium bond distance (2.506 Å) of the pristine $MoSe_2$. The equilibrium Mo–Se bond distance (2.518 Å) calculated here in the 2D monolayer Pt–$MoSe_2$ is found to be in good agreement with the previously reported results (2.537 Å) within 0.019 Å.[56] The equilibrium Pt-Se bond distance was found to be 2.623 Å. The equilibrium lattice parameters, symmetry, and average bond distances of both the 2D pristine $MoSe_2$ and Pt–$MoSe_2$ are summarized in Table 1.

After obtaining the equilibrium structure of the 2D monolayer Pt–$MoSe_2$, the electronic properties, *i.e.*, band structure and DOS were computed at the same level of theory. Following the highly symmetric *Γ–M–K–Γ* direction, like the pristine

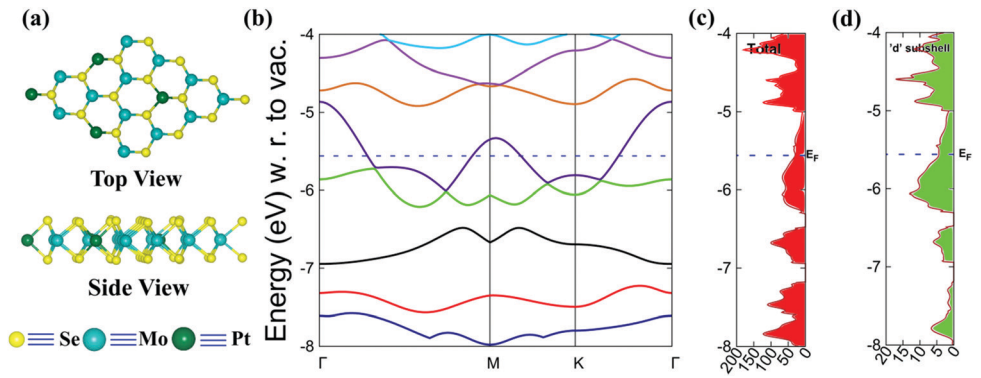

Fig. 3 The equilibrium 2D layer structure of the Pt–$MoSe_2$ material; (a) top view and side view, (b) electronic band structure, (c) total density of states (DOS), and (d) the contributing component of the d-subshell of the Pt atom in the total DOS are shown here.

Table 1 Equilibrium structural parameters and lattice parameters of both pristine $MoSe_2$ and Pt–$MoSe_2$ monolayer materials are summarized here. The lattice parameters and bond distances are expressed in Å

System	Lattice parameters	Interfacial angles in degree (°)	Space group and symmetry	Average bond distance between atoms	
				Mo–Se	Pt–Se
$MoSe_2$	$a = b = 3.234$	$\alpha = \beta = 90°$ and $\gamma = 120°$	$P\bar{6}m2$	2.506	—
Pt doped $MoSe_2$ (2×2 supercell)	$a = b = 6.738$	$\alpha = \beta = 90°$ and $\gamma = 121.7°$	$P1$	2.518	2.623

$MoSe_2$, the electronic band structures of the Pt–$MoSe_2$ have been computed and drawn with respect to the vacuum. The total eight number of bands around the Fermi level (E_F) are shown in Fig. 3b, and E_F is shown in dotted blue color. The present DFT-D calculations found that the Fermi level of this 2D Pt–$MoSe_2$ material is at −5.55 eV and the bands are overlapped around the Fermi level, as shown in Fig. 3b, resulting in a large electron density around E_F. This study shows that after the Pt doping in the pristine $MoSe_2$, the electronic band gap (E_g) has been reduced to 0 eV (whereas the E_g was found to be about 2.21 eV in the case of the 2D pristine $MoSe_2$ monolayer material). Due to this zero-band gap, electrons from the valence band can easily be transferred to the conduction band, which means that electrons are free to move in the material. Therefore, the electronic properties of the Pt–$MoSe_2$ computed by the DFT-D method reveals that it has a metallic character depicted in the band structure and the total density of states calculations, as represented in Fig. 3b and c, respectively. This metallic character is only due to the contribution of the electrons of 5d-subshell electrons of the Pt atom. To confirm this, we also computed the contributing components of the 5d-subshell electron density of the Pt atom, as displayed in Fig. 3d. Ren *et al.* and Gao *et al.* performed a similar kind of study on the 2D layered $MoSe_2$ material by doping with a single foreign atom to make it conducting for SO_2 gas adsorption, and to enhance the electrocatalytic activity for HER. From their studies, we can compare our results, which indicate that our calculations and observations on the 2D monolayer Pt–$MoSe_2$ are in good agreement with the previously reported results.[30,56] The present study showed that a large electron density is observed around the Fermi level, which makes this Pt–$MoSe_2$ material conducting. Hence, it can be used as an electrocatalyst for ORR. In other words, reducing the electronic bandgap increases the carrier concentration (*i.e.*, the concentration of electrons in the 2D Pt–$MoSe_2$ material) and enhances the electronic conductivity, which can help achieve faster electron transfer to the reactants during the ORR. Therefore, a better electrocatalytic ORR activity is expected from this material, which suggests a novel approach to enhance the ORR performance of the Pt-doped 2D monolayer $MoSe_2$ material, *i.e.*, Pt–$MoSe_2$.

After the geometry optimization, electronic property calculations, and confirming the conductivity of the Pt-doped $MoSe_2$ material, we investigated the electrocatalytic activity of the 2D monolayer Pt–$MoSe_2$ for the oxygen reduction reaction (ORR). Pt atoms were doped to activate the inert basal plane of the 2D monolayer $MoSe_2$ material to form the Pt–$MoSe_2$ 2D material, which can have high electrocatalytic activities for ORR. The intention was to find out whether this 2D Pt–$MoSe_2$ could be a promising electrode material for ORR in fuel cells. In this advancement, we explored all of the reaction steps of ORR by creating a 2×2 periodic slab model of the Pt–$MoSe_2$ material on the basis of a computational hydrogen electrode (CHE) model.[53] The O_2 reduction reaction consists of 4 electrons and 4 protons for each O_2 molecule and many other reaction intermediates, such as O* (oxygen), OH* (hydroxyl group), and OOH* (super hydroxyl group) adsorbed onto the active sites. The experimental explication of the reaction mechanism including the reaction intermediates is quite a challenging task.[17,18,57]

The computational modelling of the reaction intermediates is equally challenging because of the need to incorporate the effect of solvent on the adsorbed intermediates, the highly charged electric field in the double layer, the free energy of solvated reactants,[58] and the free energy of electrons in the solid as a function of potential.[58–63] There is a somewhat simpler way to solve this problem by linking the whole trend to the gas phase.[53] At the gas–solid interface, electrocatalytic reactions are easy to calculate. As for the gas phase species, DFT computation gives very accurate values.[64–67] The HER (hydrogen evolution reaction) and oxidation–reduction reactions are in thermal equilibrium ($2H^+ + 2e^- \leftrightarrow H_2$) with respect to a SHE (standard hydrogen electrode) at $U = 0$ V electrode potential. Therefore, at atmospheric pressure and $U = 0$ V (RHE), the free energies of the gas phase hydrogen and solvated electrons and protons in the solid are equal. Hence, the adsorption energy of any species (at $U = 0$ V), which is in equilibrium with the gas phase hydrogen, is equal to the electrochemically formed species in equilibrium with protons and electrons. Only sometimes, if necessary, a small correction can be made for the effect of water and electric field. A change in the electrode potential results in a 1 : 1 change in the free energy of electrons.[53,63,68]

At the SHE conditions when pH = 0, the neutral site, where platinum is doped, is highly active for the reaction. Among the various available sites (Se, Mo, and Pt) for the adsorption of various intermediates during ORR on TMDs, the top of the chalcogen atoms are energetically more preferable.[69] Thus, by taking into consideration the free energies of different intermediates at $U = 0$ V and pH = 0, we have calculated the change of free energy, *i.e.*, relative free energy (ΔG), in each step, and the reaction pathway with respect to the change in free energy (ΔG) is shown in Fig. 4. In the ORR pathways, we have considered a small segment of this Pt–$MoSe_2$ material for representation, where an oxygen molecule has been adsorbed.

Various steps of the ORR pathway with the change of free energy (ΔG) during the reaction are shown in Fig. 4, and the

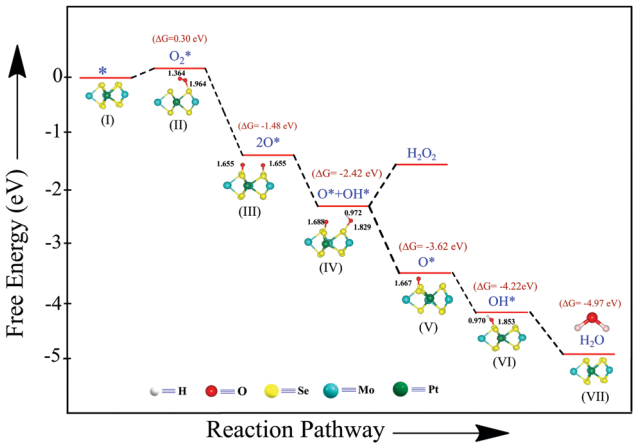

Fig. 4 Free energy diagram for the dissociative ORR pathway on the surface of the 2D Pt-doped $MoSe_2$ material with the optimized geometries of each reaction step.

intermediate structures are depicted in Fig. 5. Here, the ORR has started by the adsorption of O_2 on the surface of Pt–$MoSe_2$ by creating a bond to one of the selenium (Se) atoms attached with the Pt, as shown in Fig. 4 and 5b, noted by step-I and O_2*_Pt–$MoSe_2$ noted by step-II. It has been shown that O_2 prefers to bind with the Se atom site during the reaction, as the Se atoms are on the first layer of the 2D Pt–$MoSe_2$ surface. It was computationally found that the O_2 adsorption in the Se site is energetically more favorable than the Pt and Mo atoms by an amount of energy in the range of 0.85–1.15 eV. The first step is the adsorption of O_2 on the 2D Pt–$MoSe_2$ monolayer, where, intriguingly, the outer Se atoms of the Pt–$MoSe_2$ monolayer were found to be the active sites for O_2 activation rather than the inner Pt atoms, which is different from what was previously reported for Pt-containing ORR catalysts. The equilibrium Se-O bond distance was found to be 1.964 Å, as displayed in Fig. 4 and 5b. The equilibrium Pt-Se bond length was 2.623 Å

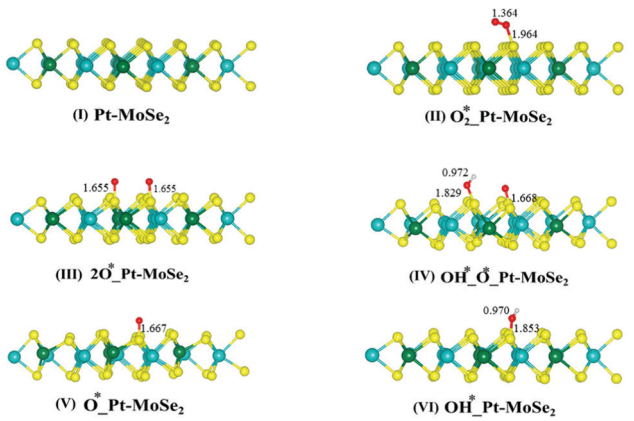

Fig. 5 Equilibrium geometries of all of the intermediates during ORR (with increased unit cell 2 × 2 in *x*-, *y*-directions, and there is no change in the *z*-direction) are depicted here: (I) Pt–$MoSe_2$; (II) O_2*_Pt–$MoSe_2$; (III) 2O*_Pt–$MoSe_2$; (IV) OH*_O*_Pt–$MoSe_2$; (V) O*_Pt–$MoSe_2$; and (f) OH*_Pt–$MoSe_2$.

in Pt–$MoSe_2$, which has been elongated by an amount of 0.468 Å after O_2 adsorption on the surface of the material during the initiation of the reaction. The equilibrium Pt–Se bond distance became 3.091 Å after the adsorption of O_2 on the surface of Pt–$MoSe_2$, making a weak bond between Se and O_2 in step-II. The value of free energy change (ΔG) of this reaction step was found to be 0.30 eV, as depicted in Fig. 4. The positive value of the free energy for this reaction step shows that the adsorption of O_2* on the Se site of Pt–$MoSe_2$ is not stable, and it will soon dissociate into 2O*. In the next step of the O_2 reduction reaction, the bond length of this activated O_2* was stretched and one oxygen atom was attached to the other Se atom near the platinum site, as given in step-III. When O_2 reaches the surface of the Pt–$MoSe_2$ monolayer, the O–O bond length is significantly stretched from 1.24 to 1.39 Å, indicating that O_2 has been effectively activated. The value of the relative Gibb's free energy in this step was about −1.48 eV. Here, the equilibrium bond lengths of both Se–O atoms were found to be around 1.655 Å. Now, two activated sites of the oxygen atoms are present with the addition of one proton, which comes from the anode side through the proton exchange membrane, and one electron, which also comes from the anode side, but through the external circuit of the PEM fuel cell. After the addition of the proton and electron on one of the activated oxygen atoms, the Se–O bond length changed to 1.829 Å from 1.654 Å (step-IV), and the value of ΔG in this step was −2.42 eV. From the free energy diagram, one can see that all of the electrochemical steps are downhill at U = 0 V, and the relative change of the Gibbs free energy in this step is about −0.94 eV. The H_2O_2 formation step is extremely endothermic (as shown in Fig. 4), suggesting that the two-electron pathway could be significantly suppressed by the $4e^-$ pathway under the normal working conditions.

Another proton (H^+) and electron (e^-) coming from the anode side were added to the OH* site, and the increment in bond length of Se–O (from 1.688 Å to 1.829 Å) after the additional proton and electron favors the removal of H_2O_2 (or H_2O) from the surface of the Pt–$MoSe_2$ electrocatalyst. In the dissociative mechanism, O_2 falls on the Pt–$MoSe_2$ surface flatly, and O–O binds to Pt in a parallel fashion. The O–O bond is activated by one-electron transfer and then cleaved into "O" (denote as 2O*), followed by protonation and electron reduction to form OH*. The change of the Gibb's free energy in this step computed at the same level of DFT-D theory is −3.62 eV. The relative change of the Gibbs free energy in this step is about −1.20 eV. Now, on the remaining activated site of O*, one proton and one electron were again added from the anode side with a free energy change of −4.22 eV. Here, the equilibrium Se–O bond distance after the addition was found to be 1.853 Å, increased from the earlier value of 1.667 Å. The Se–O equilibrium bond length is stretched. In the last step, one H_2O molecule was again removed from the surface. The computed free energy value is −4.97 eV in the last step of ORR. The whole ORR process involved a four-electron transfer mechanism. The protonation of OH* to H_2O is the potential-limiting step for the whole ORR process, with ΔG = −0.75 eV. We observed

Table 2 The change of free energy, *i.e.*, relative free energy (ΔG in eV) of all the intermediates during the oxygen reduction reaction performed on the 2D Pt-doped $MoSe_2$ is reported here

Various ORR steps	ΔG (eV)
[Pt_$MoSe_2$] → [O_2*_Pt_$MoSe_2$]	0.30
[O_2*_Pt_$MoSe_2$] → [2O*_Pt_$MoSe_2$]	−1.48
[2O*_Pt_$MoSe_2$] → [OH*_O*_Pt_$MoSe_2$]	−2.42
[OH*_O*_Pt_$MoSe_2$] → [O*_Pt_$MoSe_2$]	−3.62
[O*_Pt_$MoSe_2$] → [OH*_Pt_$MoSe_2$]	−4.22
[OH*_Pt_$MoSe_2$] → [Pt_$MoSe_2$]	−4.97

that the free energy change of each reaction step is negative, as listed in Table 2. The negative value of the change of the Gibb's free energy at each reaction step shows that all of the reaction steps are thermodynamically stable, as depicted in Fig. 4. In addition to the superior activity, the 2D Pt–$MoSe_2$ monolayer exhibits high selectivity for the $4e^-$ reduction pathway. Here, each reaction step occurs at the Pt doping site of the 2D monolayer of the Pt–$MoSe_2$ materials by making the basal plane highly active. We observe that the equilibrium bond lengths, Mo–Se, Se–O, Pt–Se, and Se–OH, change at each reaction step, as we mentioned in our earlier discussion. A detailed comparison of the lattice constants, space group symmetry and average bond lengths of each reaction step during the ORR is reported in Table 3.

We have plotted the electronic band structure and total density of states, as well as the d-subshell electron density of states of the Pt atoms in each reaction step to observe the changes of the electronic properties during the ORR, as shown in Fig. 6a–e. The electronic properties (*i.e.*, band structure and DOS), equilibrium lattice constants and equilibrium bond distances of various reaction steps (II–VI) are reported in Table 3. The high basal plane activity of the 2D monolayer Pt–$MoSe_2$ monolayer can be understood from its unique electronic property calculations, *i.e.*, electronic band structure and DOS. The electronic properties of the 2D monolayer Pt–$MoSe_2$ material are shown in Fig. 3b–d, and it was observed that the bands are overlapped around the Fermi energy (E_F) level due to the Pt-doping in the pristine $MoSe_2$, resulting in a large electron density appearing at the E_F. This shows that the electronic band gap is zero and therefore, the 2D Pt–$MoSe_2$ material has metallic character. The presence of electron density around the Fermi level was confirmed by plotting the total density of states. This electron density around the Fermi level is due to the d-subshell contribution of Pt, which was confirmed by computing the contributing component of the d-subshell electron DOS of Pt. When the reaction occurs with the adsorption of O_2 on Pt–$MoSe_2$, we can see that bands from both regions are shrinking towards the Fermi energy level. Hence, the electron density increases around the Fermi level, which is shown in Fig. 6a. We observed the same behavior in the ORR step-III, as displayed in Fig. 6b, where the oxygen molecule is splitting into two oxygen atoms by creating two bonds with the Se atoms of Pt–$MoSe_2$. In this reaction step, the bands are overlapped around E_F, and an electron density has been observed at E_F due to the d-subshell electron DOS of Pt. The band structure calculations showed that there is no electronic band gap when the protonation reaction occurred in the step-IV, *i.e.*, when hydrogen is adsorbed on the oxygen atom, as displayed in Fig. 6c. It has been found that the valence band, highlighted in green, is pushed down below E_F, and the conduction band, highlighted in blue, is moved above E_F as shown in Fig. 6c. In the next reaction step (step-V), *i.e.*, when only one oxygen atom is present on the surface of the electrocatalyst, we calculated the band structure and density of states. We observed that the band gap increased by an amount of 0.80 eV, as shown in Fig. 6d. It has been observed that both bands (valence and conduction bands) in step-V are moving away from the Fermi energy level. In the last step of the reaction (*i.e.*, step-VI), the electronic band gap was found to be 0.57 eV, as depicted in Fig. 6e.

It should be noted here that until now, many research articles have showcased electrocatalysts for the ORR. However, only a few reports on ORR have been published, and extensive efforts in both experiment and theory have been made to study the underlying mechanism of the ORR on Pt(111)-based electrocatalysts.[70–75] Other noble metals, such as Ru, Rh, Pd and Au, for example, have been reported as promising and highly efficient electrocatalysts. Among them, Pt is the most well-known active electrocatalyst for the ORR.[76] Due to the high cost of noble metals, transition metal-based compounds such

Table 3 Equilibrium structural parameters, lattice constants, and electronic band gap (E_g) parameters of the various systems of the ORR steps[a]

Reaction steps	Lattice parameters (in Å)	Interfacial angles in degree	Space group and symmetry	Electronic band gap (E_g in eV)	Average bond distance between atoms (in Å)			
					Mo–Se	Pt–Se	Se–O	Se–OH
O_2*_Pt–$MoSe_2$	a = 6.750	$\alpha = \beta$ = 90	*P*1	0	2.513	2.504	1.964	—
	b = 6.659	γ = 120.757						
2O*_Pt–$MoSe_2$	a = 6.870	$\alpha = \beta$ = 90	*P*1	0	2.523	2.561	1.655	—
	b = 6.613	γ = 119.067						
OH*_O*_Pt–$MoSe_2$	a = 6.798	$\alpha = \beta$ = 90	*P*1	0	2.529	2.615	1.668	1.829
	b = 6.668	γ = 118.480						
O*_Pt–$MoSe_2$	a = 6.703	$\alpha = \beta$ = 90	*P*1	0.80	2.538	2.484	1.667	—
	b = 6.551	γ = 116.480						
OH*_Pt–$MoSe_2$	a = 6.760	$\alpha = \beta$ = 90	*P*1	0.57	2.544	2.490	—	1.853
	b = 6.766	γ = 119.417						

[a] The lattice constants and equilibrium bond distances are expressed in Å. The band gap is expressed in eV.

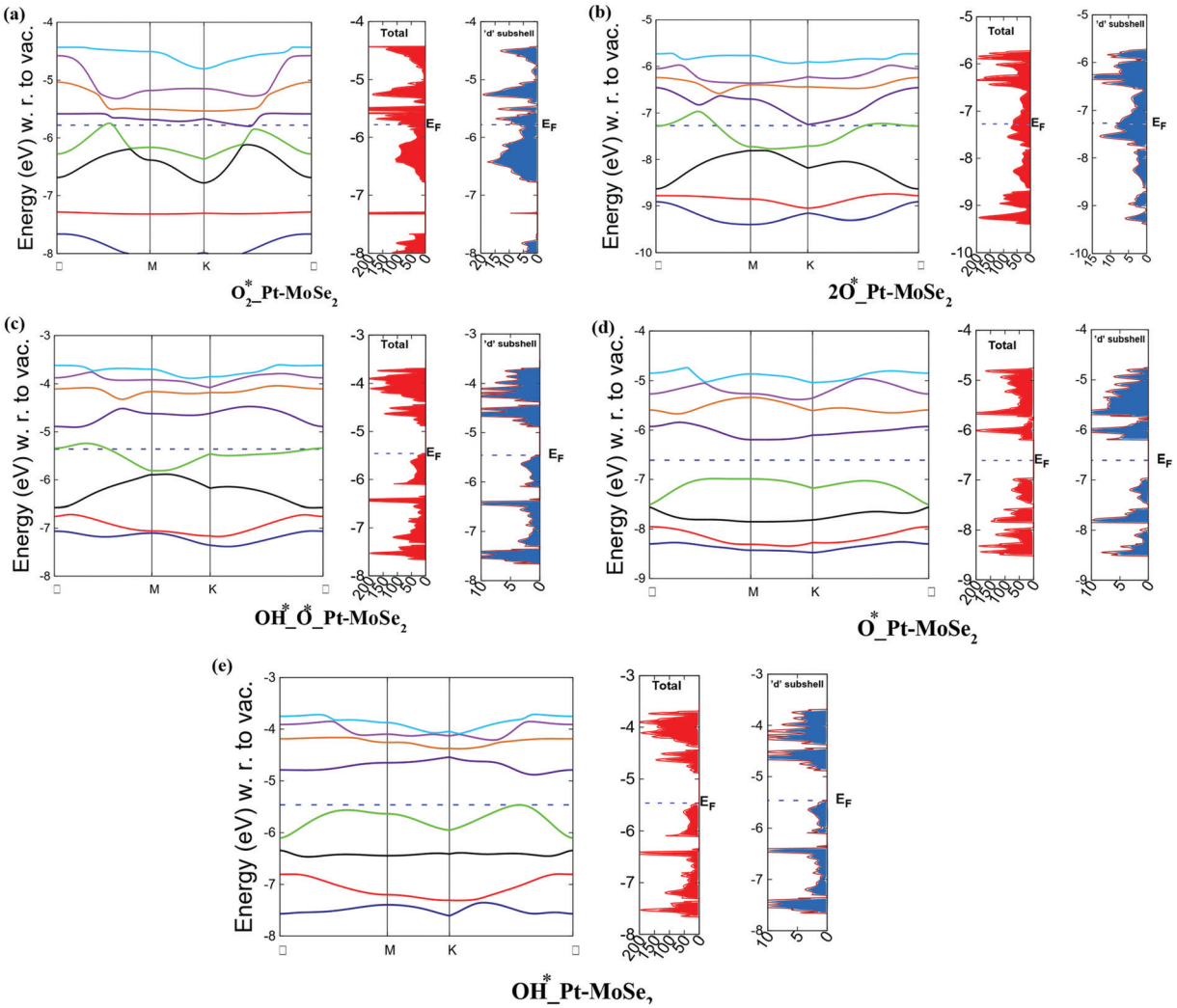

Fig. 6 Electronic band structure, total density of states, and 5d-subshell electronic density of states of the Pt atom of each reaction step during ORR on the surface of 2D Pt–$MoSe_2$ material: (a) O_2*_Pt–$MoSe_2$; (b) 2O*_Pt–$MoSe_2$; (c) OH*_O*_Pt–$MoSe_2$; (d) O*_Pt–$MoSe_2$; and (e) OH*_Pt–$MoSe_2$.

as metal oxides, metal carbides, metal nitrides, metal sulfides and metal phosphides have been utilized as alternative catalysts because they are abundant, cheap, electrochemically active and chemically stable.[77,78] The experimental limitations with the high price of these electrocatalysts contribute significantly towards the total cost, and hence hinder the mass application of these materials for ORR, especially in industries. To achieve the sustainable development of fuel cells, it is crucial to reduce the Pt-loading in Pt-based catalysts without sacrificing the catalytic activity, which thus requires the high utilization of Pt atoms. However, these 2D Pt-containing catalysts are mostly supported on other noble metals (*e.g.*, Au, Pd), rather than being free-standing or dispersed genuine 2D structures, which is not favorable for efficient catalysis. Our present study found that the 2D pristine $MoSe_2$ has semiconducting characteristics. However, the 2D monolayer Pt–$MoSe_2$ is metallic due to the existence of a doped-Pt layer in the system. Remarkably, the basal plane of the Pt–$MoSe_2$ monolayer exhibits superior catalytic activity and high four-electron (4e) selectivity toward electrochemical ORR, making it promising for applications in fuel cells. The potential energy surface (PES) of the Pt–$MoSe_2$ monolayer material shows similar trends like the pristine Pt(111) for ORR, and the changes of free energy (ΔG) during ORR on the surfaces of 2D monolayer Pt–$MoSe_2$ are in reasonable accordance with the values of ΔG on Pt(111).[73] The protonation of OH* to H_2O on the surfaces of the 2D Pt–$MoSe_2$ monolayer material is the potential-limiting step for the whole ORR process with the change of free energy about -0.75 eV ($\Delta G = -0.75$ eV), which is comparable to the value of the Pt(111) and PtTe electrocatalysts.[12,73] In particular, the CHE model-based computations demonstrated that the 2D Pt–$MoSe_2$ monolayer is a promising ORR catalyst candidate with an outstanding catalytic activity, like Pt(111) and PtTe.[12,73] It is expected that this material is a candidate to substitute the Pt electrodes, and it could be realized in the laboratory and be utilized as an ORR catalyst in the near future.

Conclusion

In the present study, we computationally studied the structural and electronic properties, such as the electronic band structure and density of states of both pristine 2D $MoSe_2$ and Pt–$MoSe_2$ materials. It was found that the pristine 2D monolayer $MoSe_2$ is a direct band gap semiconductor with a band gap of around 2.21 eV, and there was no electronic density around the Fermi energy level, meaning that this material is intrinsically inert toward the catalytic reduction of oxygen in ORR. We doped single platinum atom in the pristine 2D $MoSe_2$, and studied the resulting electronic properties. We observed that the electronic band gap was reduced from 2.21 eV to '0' eV. This reduction in band gap was due to the 5d-subshell contribution of the Pt atom, which was confirmed by the d-subshell electron density of states computations of the platinum atom. We observed the presence of a large electronic density around the Fermi energy level, indicating that the Pt–$MoSe_2$ monolayer is metallic with considerable electronic states at the Fermi energy level. As a result, electrons from the valence band can be transferred easily to the conduction band. Based on these observations, we predict that the 2D monolayer Pt–$MoSe_2$ material can be used as an efficient electrocatalyst for ORR. In particular, the CHE model-based computations demonstrated that the Pt–$MoSe_2$ monolayer is a promising ORR catalyst candidate with outstanding catalytic activity and high 4e reduction pathway selectivity. To confirm our prediction, we computationally studied the oxygen reduction reaction performance on the surface of the 2D monolayer Pt–$MoSe_2$ material by exploring all of the reaction steps of ORR with the relative free energies. This study showed that all of the steps are thermodynamically and energetically favorable and feasible. Our present observation revealed that the Pt-doped 2D $MoSe_2$ monolayer is a promising electrode material to be used in fuel cell and battery technology to efficiently perform the oxygen reduction reaction with a significant enhancement in the reaction kinetics. This research indicates that the 2D monolayer Pt–$MoSe_2$ could be accomplished in the laboratory, and be employed as ORR catalyst in the near future for industrial applications.

Author contributions

Dr Pakhira developed the complete idea of this current research work, and he and Mr Shrish Nath Upadhyay computationally studied the electronic structures and properties of the Pt-doped $MoSe_2$. Dr Pakhira explored the whole reaction pathways, intermediate states and reactions barriers, and he explained the ORR mechanism by the DFT calculations. Quantum calculations and theoretical models were designed and performed by Dr Pakhira and Mr Shrish Nath Upadhyay. Dr Pakhira wrote the whole manuscript, and prepared all of the tables and figures in the manuscript. Mr Shrish Nath Upadhyay helped Dr Pakhira in organizing the manuscript.

Conflicts of interest

There are no conflicts to declare.

Acknowledgements

This work was financially supported by the Science and Engineering Research Board-Department of Science and Technology (SERB-DST), Government of India under Grant No. ECR/2018/000255. Dr Srimanta Pakhira acknowledges the SERB-DST, Government of India for providing his Early Career Research Award (ECRA) under the project number ECR/2018/000255. Dr Pakhira also thanks the SERB-DST for providing the highly prestigious Ramanujan Faculty Fellowship under the scheme number SB/S2/RJN-067/2017. Mr Upadhyay thanks Indian Institute of Technology Indore (IIT Indore) and MHRD, Govt. of India for providing his doctoral fellowship. The author would like to acknowledge the SERB-DST for providing the computing cluster and programs, and IIT Indore for providing the basic infrastructure to conduct this research work.

References

1 P. G. Bruce, S. A. Freunberger, L. J. Hardwick and J. M. Tarascon, *Nat. Mater.*, 2012, **11**, 19–29.
2 L. Carrette, K. A. Friedrich and U. Stimming, *ChemPhysChem*, 2000, **1**, 162–193.
3 H. A. Gasteiger, S. S. Kocha, B. Sompalli and F. T. Wagner, *Appl. Catal., B*, 2005, **56**, 9–35.
4 W. Yu, M. D. Porosoff and J. G. Chen, *Chem. Rev.*, 2012, **112**, 5780–5817.
5 A. Kongkanand and M. F. Mathias, *J. Phys. Chem. Lett.*, 2016, **7**, 1127–1137.
6 Y. Nie, L. Li and Z. Wei, *Chem. Soc. Rev.*, 2015, **44**, 2168–2201.
7 W. Niu, S. Pakhira, K. Marcus, Z. Li, J. L. Mendoza-Cortes and Y. Yang, *Adv. Energy Mater.*, 2018, **8**, 1800480.
8 J. Hui, S. Pakhira, R. Bhargava, Z. J. Barton, X. Zhou, A. J. Chinderle, J. L. Mendoza-Cortes and J. Rodríguez-López, *ACS Nano*, 2018, **12**, 2980–2990.
9 N. M. Markovic, T. J. Schmidt, V. Stamenkovic and P. N. Ross, *Fuel Cells*, 2001, **1**, 105–116.
10 M. K. Debe, *Nature*, 2012, **486**, 43–51.
11 V. Tripkovic and T. Vegge, *J. Phys. Chem. C*, 2017, **121**, 26785–26793.
12 Y. Wang, Y. Li and T. Heine, *J. Am. Chem. Soc.*, 2018, **140**, 12732–12735.
13 X. Wang, Z. Li, Y. Qu, T. Yuan, W. Wang, Y. Wu and Y. Li, *Chem*, 2019, **5**, 1486–1511.
14 D. Deng, K. S. Novoselov, Q. Fu, N. Zheng, Z. Tian and X. Bao, *Nat. Nanotechnol.*, 2016, **11**, 218–230.
15 H. Zhang and R. Lv, *J. Mater.*, 2018, **4**, 95–107.
16 D. Zhao, Z. Zhuang, X. Cao, C. Zhang, Q. Peng, C. Chen and Y. Li, *Chem. Soc. Rev.*, 2020, **49**, 2215–2264.
17 J. Greeley, I. E. L. Stephens, A. S. Bondarenko, T. P. Johansson, H. A. Hansen, T. F. Jaramillo, J. Rossmeisl, I. Chorkendorff and J. K. Nørskov, *Nat. Chem.*, 2009, **1**, 552–556.
18 I. E. L. Stephens, A. S. Bondarenko, U. Grønbjerg, J. Rossmeisl and I. Chorkendorff, *Energy Environ. Sci.*, 2012, **5**, 6744–6762.

19 J. Zhang, M. B. Vukmirovic, Y. Xu, M. Mavrikakis and R. R. Adzic, *Angew. Chem., Int. Ed.*, 2005, **44**, 2132–2135.
20 N. A. Mayorova, O. M. Zhigalina, V. G. Zhigalina and O. A. Khazova, *Russ. J. Electrochem.*, 2014, **50**, 223–230.
21 A. Kjekshus, F. Grønvold, P. M. Jørgensen and S. Refn, *Acta Chem. Scand.*, 1959, **13**, 1767–1774.
22 S. Manzeli, D. Ovchinnikov, D. Pasquier, O. V. Yazyev and A. Kis, *Nat. Rev. Mater.*, 2017, **2**, 17033.
23 P. Mirõ, M. Ghorbani-Asl and T. Heine, *Angew. Chem., Int. Ed.*, 2014, **53**, 3015–3018.
24 Y. Zhao, J. Qiao, P. Yu, Z. Hu, Z. Lin, S. P. Lau, Z. Liu, W. Ji and Y. Chai, *Adv. Mater.*, 2016, **28**, 2399–2407.
25 Z. Wang, Q. Li, F. Besenbacher and M. Dong, *Adv. Mater.*, 2016, **28**, 10224–10229.
26 Y. Lei, S. Pakhira, K. Fujisawa, X. Wang, O. O. Iyiola, N. Perea López, A. Laura Elías, L. Pulickal Rajukumar, C. Zhou, B. Kabius, N. Alem, M. Endo, R. Lv, J. L. Mendoza-Cortes and M. Terrones, *ACS Nano*, 2017, **11**, 5103–5112.
27 K. Liang, S. Pakhira, Z. Yang, A. Nijamudheen, L. Ju, M. Wang, C. I. Aguirre-Velez, G. E. Sterbinsky, Y. Du, Z. Feng, J. L. Mendoza-Cortes and Y. Yang, *ACS Catal.*, 2019, **9**, 651–659.
28 S. N. Upadhyay, J. A. K. Satrughna and S. Pakhira, *Emergent Mater.*, 2021, 1–20.
29 A. Eftekhari, *Appl. Mater. Today*, 2017, **8**, 1–17.
30 D. Gao, B. Xia, C. Zhu, Y. Du, P. Xi, D. Xue, J. Ding and J. Wang, *J. Mater. Chem. A*, 2018, **6**, 510–515.
31 J. G. Chen, C. A. Menning and M. B. Zellner, *Surf. Sci. Rep.*, 2008, **63**, 201–254.
32 G. C. Wang, L. Jiang, X. Y. Pang and J. Nakamura, *J. Phys. Chem. B*, 2005, **109**, 17943–17950.
33 L. Liu and A. Corma, *Chem. Rev.*, 2018, **118**, 4981–5079.
34 J. Yan, J. Xia, Q. Zhang, B. Zhang and B. Wang, *Materials*, 2018, **11**, 1–13.
35 K. A. Baseden and J. W. Tye, *J. Chem. Educ.*, 2014, **91**, 2116–2123.
36 A. D. Becke, *J. Chem. Phys.*, 1993, **98**, 5648–5652.
37 R. Dovesi, F. Pascale, B. Civalleri, K. Doll, N. M. Harrison, I. Bush, P. D'Arco, Y. Noël, M. Rérat, P. Carbonnière, M. Causà, S. Salustro, V. Lacivita, B. Kirtman, A. M. Ferrari, F. S. Gentile, J. Baima, M. Ferrero, R. Demichelis and M. De La Pierre, *J. Chem. Phys.*, 2020, **152**, 204111.
38 S. Pakhira, C. Sahu, K. Sen and A. K. Das, *Chem. Phys. Lett.*, 2012, **549**, 6–11.
39 K. Liang, S. Pakhira, Z. Yang, A. Nijamudheen, L. Ju, M. Wang, C. I. Aguirre-Velez, G. E. Sterbinsky, Y. Du, Z. Feng, J. L. Mendoza-Cortes and Y. Yang, *ACS Catal.*, 2019, **9**, 651–659.
40 J. Laun, D. Vilela Oliveira and T. Bredow, *J. Comput. Chem.*, 2018, **39**, 1285–1290.
41 S. Pakhira and J. L. Mendoza-Cortes, *J. Phys. Chem. C*, 2018, **122**, 4768–4782.
42 S. Pakhira and J. L. Mendoza-Cortes, *Phys. Chem. Chem. Phys.*, 2019, **21**, 8785–8796.
43 S. Pakhira, *RSC Adv.*, 2019, **9**, 38137–38147.
44 S. Pakhira, K. P. Lucht and J. L. Mendoza-Cortes, *J. Phys. Chem. C*, 2017, **121**, 21160–21170.
45 S. Pakhira, K. P. Lucht and J. L. Mendoza-Cortes, *J. Chem. Phys.*, 2018, **148**, 064707.
46 N. Sinha and S. Pakhira, *ACS Appl. Electron. Mater.*, 2021, **3**, 720–732.
47 S. Pakhira and J. L. Mendoza-Cortes, *J. Phys. Chem. C*, 2020, **124**, 6454–6460.
48 S. Pakhira, B. S. Lengeling, O. Olatunji-Ojo, M. Caffarel, M. Frenklach and W. A. Lester, *J. Phys. Chem. A*, 2015, **119**, 4214–4223.
49 S. Pakhira, R. I. Singh, O. Olatunji-Ojo, M. Frenklach and W. A. Lester, *J. Phys. Chem. A*, 2016, **120**, 3602–3612.
50 R. Puttaswamy, R. Nagaraj, P. Kulkarni, H. K. Beere, S. N. Upadhyay, R. G. Balakrishna, N. Sanna Kotrappanavar, S. Pakhira and D. Ghosh, *ACS Sustainable Chem. Eng.*, 2021, **9**, 3985–3995.
51 H. J. Monkhorst and J. D. Pack, *Phys. Rev. B: Condens. Matter Mater. Phys.*, 1976, **13**, 5188–5192.
52 K. Momma and F. Izumi, *J. Appl. Crystallogr.*, 2011, **44**, 1272–1276.
53 J. K. Nørskov, J. Rossmeisl, A. Logadottir, L. Lindqvist, J. R. Kitchin, T. Bligaard and H. Jónsson, *J. Phys. Chem. B*, 2004, **108**, 17886–17892.
54 P. B. James and M. T. Lavik, *Acta Crystallogr.*, 1963, **16**, 1183.
55 J. Kang, J. Li, S. S. Li, J. B. Xia and L. W. Wang, *Nano Lett.*, 2013, **13**, 5485–5490.
56 J. Ren, Y. Xue and L. Wang, *Chem. Phys. Lett.*, 2019, **733**, 136631.
57 A. A. Gewirth and M. S. Thorum, *Inorg. Chem.*, 2010, **49**, 3557–3566.
58 O. Sugino, I. Hamada, M. Otani, Y. Morikawa, T. Ikeshoji and Y. Okamoto, *Surf. Sci.*, 2007, **601**, 5237–5240.
59 A. B. Anderson and T. V. Albu, *J. Am. Chem. Soc.*, 1999, **121**, 11855–11863.
60 M. N. Jean-Sebastien Filhol, *Angew. Chem., Int. Ed.*, 2006, **45**, 402–406.
61 E. Skúlason, V. Tripkovic, M. E. Björketun, S. Gudmundsdóttir, G. Karlberg, J. Rossmeisl, T. Bligaard, H. Jónsson and J. K. Nørskov, *J. Phys. Chem. C*, 2010, **114**, 18182–18197.
62 P. Taylor, A. Gasteiger and W. Reitz, *Mater. Manuf. Processes*, 2007, **2**, 789.
63 J. Rossmeisl, E. Skúlason, M. E. Björketun, V. Tripkovic and J. K. Nørskov, *Chem. Phys. Lett.*, 2008, **466**, 68–71.
64 P. Nieto, E. Pijper, D. Barredo, G. Laurent, R. A. Olsen, E. J. Baerends, G. J. Kroes and D. Farías, *Science*, 2006, **312**, 86–89.
65 J. K. Nørskov, T. Bligaard, A. Logadottir, S. Bahn, L. B. Hansen, M. Bollinger, H. Bengaard, B. Hammer, Z. Sljivancanin, M. Mavrikakis, Y. Xu, S. Dahl and C. J. H. Jacobsen, *J. Catal.*, 2002, **209**, 275–278.
66 K. Reuter, D. Frenkel and M. Scheffler, *Phys. Rev. Lett.*, 2004, **93**, 1–4.
67 K. Honkala, A. Hellman, I. N. Remediakis, A. Logadottir, A. Carlsson, S. Dahl, C. H. Christensen and J. K. Nørskov, *Science*, 2005, **307**, 555–558.

68 G. S. Karlberg, J. Rossmeisl and J. K. Nørskov, *Phys. Chem. Chem. Phys.*, 2007, **9**, 5158–5161.
69 S. Zhao, K. Wang, X. Zou, L. Gan, H. Du, C. Xu, F. Kang, W. Duan and J. Li, *Nano Res.*, 2019, **12**, 925–930.
70 I. E. L. Stephens, A. S. Bondarenko, F. J. Perez-alonso, F. Calle-vallejo, L. Bech, T. P. Johansson, A. K. Jepsen, R. Frydendal, B. P. Knudsen, J. Rossmeisl and I. Chorkendor, *J. Am. Chem. Soc.*, 2011, **133**, 5485–5491.
71 M. H. Shao, P. Liu and R. R. Adzic, *J. Am. Chem. Soc.*, 2006, **128**, 7408–7409.
72 U. Benedikt, W. B. Schneider and A. A. Auer, *Phys. Chem. Chem. Phys.*, 2013, **15**, 2712–2724.
73 S. Liu, M. G. White and P. Liu, *J. Phys. Chem. C*, 2016, **120**, 15288–15298.
74 T. Ikeshoji and M. Otani, *Phys. Chem. Chem. Phys.*, 2017, **19**, 4447–4453.
75 K. Y. Yeh, S. A. Wasileski and M. J. Janik, *Phys. Chem. Chem. Phys.*, 2009, **11**, 10108–10117.
76 Y. Sun, C. Li and G. Shi, *J. Mater. Chem.*, 2012, **22**, 12810–12816.
77 S. Dou, L. Tao, J. Huo, S. Wang and L. Dai, *Energy Environ. Sci.*, 2016, **9**, 1320–1326.
78 C. H. Lai, M. Y. Lu and L. J. Chen, *J. Mater. Chem.*, 2012, **22**, 19–30.